

Lattice dynamics and microscopic mechanisms of the spontaneous magnetodielectric effect in the antiferromagnetic fluoroperovskites KCoF_3 and RbCoF_3

R. M. Dubrovin,^{1,*} N. V. Siverin,¹ P. P. Syrnikov,¹ N. N. Novikova,² K. N. Boldyrev,² and R. V. Pisarev¹

¹*Ioffe Institute, Russian Academy of Sciences, 194021 St.-Petersburg, Russia*

²*Institute of Spectroscopy, Russian Academy of Sciences, 108840 Moscow, Troitsk, Russia*



(Received 22 May 2019; revised manuscript received 11 July 2019; published 26 July 2019)

Experimental studies demonstrate that the low-frequency dielectric permittivity of many magnetic materials is sensitive to the spin ordering, but the microscopic mechanisms of the observed phenomena still remain poorly understood. Here we report on the study of lattice dynamics and the spontaneous magnetodielectric effect using far-infrared and low-frequency dielectric spectroscopy in the model fluoroperovskites KCoF_3 and RbCoF_3 in the temperature range of 5–300 K, which includes the antiferromagnetic transition at $T_N = 115$ K and 101 K, respectively. We show that the dielectric permittivity is mainly defined by the transverse TO and longitudinal LO infrared-active phonons and their specific contributions were determined. The anomalous growth of the low-frequency dielectric permittivity observed in KCoF_3 with cooling is explained by the increase of the LO-TO splitting of the lowest frequency phonon caused by about 7 cm^{-1} softening. An important conclusion is that, microscopically, the spontaneous magnetodielectric effect is caused by the frequency shifts of only those TO and LO phonons which change the 180° angle of the superexchange $\text{Co}^{2+} - \text{F}^{1-} - \text{Co}^{2+}$ pathway, thus resulting in its modulation due to the spin-phonon coupling. The observed anomalous softening of the lowest frequency phonon and increase of the low-frequency dielectric permittivity were interpreted as a manifestation of the ferroelectric instability in cubic fluoroperovskites.

DOI: [10.1103/PhysRevB.100.024429](https://doi.org/10.1103/PhysRevB.100.024429)

I. INTRODUCTION

Perovskite materials play a very important role in fundamental science and modern technology [1]. They exhibit an astonishing diversity of intriguing physical phenomena in their electric [2], piezoelectric [3], ferroelectric [4], magnetic [5], multiferroic [6], magnetoelectric [7], superconducting [8], photovoltaic [9], and other properties. However, despite intense research of perovskite materials, many fundamental microscopic problems related to the coupling between the lattice, charge, spin, and orbital degrees of freedom remain unsolved, which delays their further widescale use in technologically efficient devices.

The most widely studied perovskite materials are oxides but another group of halide perovskites demonstrates a variety of specific properties; see, e.g., Refs. [10,11]. Fluoroperovskites are materials with a chemical formula AMF_3 , where A^{1+} is an alkali metal ion and M^{2+} is a bivalent metal ion. The ideal perovskite structure is cubic but in many cases it is distorted even at room temperature and atmospheric pressure. Fluoroperovskites adopt different crystal structures which are usually consistent with their tolerance factor t [12] because they are more ionic in comparison to oxides. For example, fluoroperovskites with $t < 0.78$ adopt the trigonal structure, in the range of $0.78 < t < 0.88$ the orthorhombic phase is stabilized, the cubic phase is adopted in the range of $0.88 < t < 1.00$, and the hexagonal structure is realized for $1.00 < t < 1.08$ [13].

Recent *ab initio* calculations predicted that orthorhombic fluoroperovskites may possess ferroelectric instability in their high-symmetry cubic phase and the degree of instability correlates with the tolerance factor t [14,15]. These predictions were recently experimentally confirmed for NaMnF_3 with the lowest value of $t = 0.78$ and it was shown that the strained thin films are ferroelectric at room temperature [16]. Moreover, the dielectric measurements showed that the single crystal of NaMnF_3 is an incipient ferroelectric with a very large magnetodielectric effect [17]. These intriguing theoretical and experimental results put on the agenda the necessity of further more detailed studies of fluoroperovskites with a view to get a deeper understanding of the interaction mechanisms between the lattice and magnetic subsystems.

In this paper, we present results of experimental studies of the lattice dynamics in the model cubic antiferromagnetic fluoroperovskites KCoF_3 and RbCoF_3 . Their structural, magnetic, optical, and other properties were widely studied but no results on temperature behavior of their dielectric and magnetodielectric properties were reported so far. Our investigations showed a drastically different temperature behavior of the low-frequency dielectric permittivity ϵ_0 in these two very similar crystals, which made us undertake an in-depth study of the lattice dynamics and its coupling with the magnetic subsystem. A number of far-infrared experiments on KCoF_3 have been previously published [18–20] but no such data are available for RbCoF_3 . However, the detailed study of the lattice dynamics and its coupling with magnetic subsystems in a wide temperature range have not been reported so far. We show that the growth of the low-frequency dielectric permittivity occurs only in KCoF_3 , which we assigned to the

*dubrovin@mail.ioffe.ru

increase of LO-TO splitting of the lowest frequency phonon ω_1 . We prove that the spontaneous MD effect observed in both crystals is caused by the renormalization of the phonon frequencies below the Néel temperature T_N due to the spin-phonon coupling.

II. THEORETICAL BACKGROUND

A. Temperature dependence of the low-frequency dielectric permittivity and the spontaneous magnetodielectric effect

The low-frequency dielectric permittivity ε_0 is a fundamental integral characteristic of solids which is intrinsically related to the lattice dynamics. The temperature behavior of the low-frequency dielectric permittivity $\varepsilon_0(T)$ of normal anharmonic dielectric crystals without any structural, ferroelectric, or magnetic phase transitions is characterized by a slight decrease of ε_0 with cooling. Typically, it is described by an Einstein-type function when the following equation is applied [21–25]:

$$\varepsilon_0(T) = \varepsilon_0(0) + \frac{A}{e^{(\hbar\omega^*/k_B T)} - 1}, \quad (1)$$

where $\varepsilon_0(0)$ and A are constants and ω^* is the frequency at zero temperature of the effective infrared (IR) active optical phonon with a dominant dielectric strength. This type of temperature dependence was observed in a large number of ionic crystals, see, e.g., Refs. [26–29].

In contrast, in the incipient ferroelectrics, e.g., SrTiO₃ [30], EuTiO₃ [31], and NaMnF₃ [17], the low-frequency dielectric permittivity increases with cooling and saturates at low temperatures without ferroelectric phase transition. In this case, the temperature dependence of $\varepsilon_0(T)$ obeys the Barrett equation [32]

$$\varepsilon_0(T) = \varepsilon_B + \frac{C_B}{(T_1/2) \coth(T_1/2T) - T_0}, \quad (2)$$

where T_0 equals the Curie-Weiss temperature in the classical limit, T_1 marks the temperature below which quantum fluctuations become important, and ε_B , C_B are constants. The growth of the dielectric permittivity with cooling is related to a softening of the IR active phonons.

The influence of magnetic ordering on the low-frequency dielectric permittivity ε_0 in the absence of any external magnetic field is regarded as the spontaneous magnetodielectric (MD) effect, which in the simplest case of a single exchange interaction is dominated by the spin-pair correlation function $\langle S_i \cdot S_j \rangle$ between nearest-neighbor sites [31,33]. The temperature dependence of the spontaneous MD effect can be expressed as

$$\Delta\varepsilon_0^{\text{MD}}(T) = \varepsilon_0^{\text{m}}(T) - \varepsilon_0(T) = \alpha \langle S_i \cdot S_j \rangle, \quad (3)$$

where $\varepsilon_0^{\text{m}}(T)$ and $\varepsilon_0(T)$ describe the temperature dependence of the low-frequency dielectric permittivity with and without the magnetic ordering, respectively, and α is a coefficient defining the spontaneous MD effect. In the case of multisublattice structures in which magnetic ordering is defined by several exchange interactions, more complex equations should be applied. Neglecting the short-range magnetic order, the spin-pair correlation function is proportional to M^2 , where M

is the magnetic order parameter, which can be calculated using the Brillouin function [34].

Among a wide variety of space- and time-symmetry-restricted physical phenomena in multiferroics and magnetoelectrics, the spontaneous MD effect is allowed in all dielectrics and semiconductors below the magnetic ordering temperature. In its essence, the spontaneous MD effect is an integral characterization of the coupling between the lattice and magnetic subsystems. The spontaneous MD effect was experimentally observed in many magnetic materials, e.g., in K₂CoF₄ [33], KNiF₃ [35], MnO [22], MnF₂ [24], EuTiO₃ [31], SeCuO₃ [36], YMnO₃ [37], NaMnF₃ [17], and in several others. Analysis of these studies shows that in most magnetic materials, the spontaneous MD effect is negative and leads to a decrease in the low-frequency dielectric permittivity below the magnetic ordering temperature. Typically, the values of the spontaneous MD effect are on the order of several percent. It is important to distinguish that the magnetic field induced MD effect can be observed both below and above the magnetic ordering temperature. Moreover, there are no symmetry restrictions of the magnetic-field-induced MD effects even in paramagnetic materials. However, spontaneous MD effects are usually larger than the field-induced ones.

B. Modeling of the far-infrared reflectivity spectra

The reflectivity $R(\omega)$ of light from an interface obeys the Fresnel's equations, which in the case of the normal incidence on the sample surface can be written as follows:

$$R(\omega) = r(\omega)r^*(\omega) = \left| \frac{\sqrt{\varepsilon(\omega)} - \sqrt{\mu(\omega)}}{\sqrt{\varepsilon(\omega)} + \sqrt{\mu(\omega)}} \right|^2, \quad (4)$$

where $r(\omega)$ is the complex reflection coefficient, $\varepsilon(\omega)$ is the dielectric function, and $\mu(\omega)$ is the magnetic permeability. The latter in most compounds has negligible influence on the reflectivity spectra and is usually set to unity $\mu(\omega) \approx 1$. Equation (4) is valid for all isotropic homogeneous materials in the limit of linear classical electrodynamics [38].

The complex dielectric permittivity $\varepsilon(\omega)$ of crystals is determined primarily by polar optical phonons and may be calculated using a generalized factorized function [39,40]

$$\varepsilon(\omega) = \varepsilon_\infty \prod_j \frac{\omega_{j\text{LO}}^2 - \omega^2 + i\gamma_{j\text{LO}}\omega}{\omega_{j\text{TO}}^2 - \omega^2 + i\gamma_{j\text{TO}}\omega}, \quad (5)$$

where ε_∞ is the high-frequency dielectric permittivity resulting from the electronic structure and can be experimentally determined from the reflectivity or the index of refraction at frequencies higher than the phonon frequencies; $\omega_{j\text{LO}}$, $\omega_{j\text{TO}}$, $\gamma_{j\text{LO}}$, and $\gamma_{j\text{TO}}$ correspond to longitudinal (LO) and transverse (TO) frequencies (ω_j) and dampings (γ_j) of j th IR active phonon, respectively. When the phonon modes are well separated, fitting of the reflectivity spectrum by using Eqs. (4) and (5) provides a reliable determination of the model parameters.

Note that the factorized form of the complex dielectric function $\varepsilon(\omega)$ [Eq. (5)] allows one to get to a better fitting of the reflectivity spectra in the case of a large LO-TO splitting compared with the classical Lorentz oscillator model for the dielectric function with the three independent

parameters [39,41–43]

$$\varepsilon(\omega) = \varepsilon_\infty + \sum_j \frac{\Delta\varepsilon_j \omega_{j\text{TO}}^2}{\omega_{j\text{TO}}^2 - \omega^2 + i\gamma_{j\text{TO}}\omega}, \quad (6)$$

where $\Delta\varepsilon_j$ is the dielectric strength of the j th phonon and the other parameters have the same meaning as in Eq. (5).

For the factorized form of the complex dielectric permittivity [Eq. (5)], the dielectric strength $\Delta\varepsilon_j$ of a particular j th phonon can be obtained from an expression [44]:

$$\Delta\varepsilon_j = \frac{\varepsilon_\infty}{\omega_{j\text{TO}}^2} \frac{\prod_k \omega_{k\text{LO}}^2 - \omega_{j\text{TO}}^2}{\prod_{k \neq j} \omega_{k\text{TO}}^2 - \omega_{j\text{TO}}^2}. \quad (7)$$

Each IR active phonon contributes additively to the optical static dielectric permittivity, $\varepsilon_0^{\text{opt}}$, in accordance with an expression

$$\varepsilon_0^{\text{opt}} = \varepsilon_\infty + \sum_j \Delta\varepsilon_j. \quad (8)$$

The dielectric strength $\Delta\varepsilon_j$ of the j th phonon can be related to an effective ionic plasma frequency $\Omega_{j\text{P}}$ as

$$\Omega_{j\text{P}}^2 = \Delta\varepsilon_j \omega_{j\text{TO}}^2. \quad (9)$$

In a multimode system, the value of effective ionic plasma frequency is related to the LO-TO splitting and effective charges according to the following equation [43–45]:

$$\Omega_{\Sigma\text{P}}^2 = \sum_j \Omega_{j\text{P}}^2 = \varepsilon_\infty \sum_j \omega_{j\text{LO}}^2 - \omega_{j\text{TO}}^2 = \frac{\varepsilon_\infty}{V\varepsilon_{\text{vac}}} \sum_k \frac{(Z_k^*e)^2}{m_k}, \quad (10)$$

where V denotes the unit cell volume, ε_{vac} is the dielectric permittivity of the free space, and Z_k^*e is the effective charge of the k th ion with the mass m_k contributing to a specific polar mode. The summation on the right-hand side is taken over all different ions in the unit cell. In the case of fluoroperovskites, the charge neutrality of the unit cell requires that

$$Z_A^* + Z_M^* + 3Z_F^* = 0. \quad (11)$$

In ternary compounds, Eqs. (10) and (11) do not allow unambiguous determination of the charges of all ions. In this case, specific assumptions concerning the effective charge of at least one ion have to be made [41,43].

C. Anharmonic effects and spin-phonon coupling

For evaluating the influence of the magnetic ordering on the phonons, we have to distinguish contributions from the purely nonmagnetic anharmonic origin and those related to the magnetic ordering. In normal anharmonic crystals, one expects that on decreasing temperature, the phonon frequencies should moderately increase, whereas dampings decrease. The frequency ω_j of a j th phonon of the structurally stable crystals without any phase transitions depends on the temperature due to anharmonic three- and four-phonon processes and is specified by an expression [46,47]

$$\omega_j(T) = \omega_{j0} + A_j \left(1 + \frac{2}{e^{\hbar\omega_{j0}/2k_B T} - 1} \right) + B_j \left(1 + \frac{3}{e^{\hbar\omega_{j0}/3k_B T} - 1} + \frac{3}{(e^{\hbar\omega_{j0}/3k_B T} - 1)^2} \right), \quad (12)$$

where ω_{j0} is the pure harmonic phonon frequency, A_j and B_j are coefficients describing three- and four-phonon anharmonic processes, respectively.

For describing the temperature dependence of the IR active phonon frequencies due to conventional anharmonic effects, a simpler model is also used, assuming that [48]

$$\omega_j = \omega_{j0} \left(1 - \frac{c_j}{e^{\theta_D/T} - 1} \right), \quad (13)$$

where θ_D is the Debye temperature, determined by an average of all IR active phonon frequencies, and c_j are parameters defining the anharmonic strength of the j th phonon.

In the molecular field treatment, the phonon frequency shift due to magnetic ordering is defined by the spin-phonon coupling which is proportional to the spin-pair correlation function and can be expressed as [49]

$$\omega_{\text{SP}} = \omega_0 + \lambda \langle S_i \cdot S_j \rangle, \quad (14)$$

where ω_0 is the phonon frequency in the absence of spin-phonon coupling, $\langle S_i \cdot S_j \rangle$ denotes a statistical-mechanical average for exchange coupled spins, and λ is the spin-phonon coupling constant. The λ constant is a second spatial derivative of the exchange terms which takes a different value for each phonon and may be positive or negative [49]. The temperature dependence of the spin correlation function $\langle S_i \cdot S_j \rangle$ is calculated using the appropriate Brillouin function similar to the previously described spontaneous MD effect in Sec. II A.

III. EXPERIMENTAL DETAILS

Cobalt fluoroperovskites KCoF_3 and RbCoF_3 have an ideal cubic perovskite structure at room temperature with the space group $Pm\bar{3}m$ (#221, $Z = 1$), and the lattice parameters $a = 4.069 \text{ \AA}$ and 4.127 \AA , and relevant tolerance factors $t = 0.94$ and 1.0 , respectively [13,50,51]. The unit cell contains five atoms occupying the Wyckoff positions 1a (0, 0, 0) for K and Rb, 1b ($\frac{1}{2}, \frac{1}{2}, \frac{1}{2}$) for Co, and 3c (0, $\frac{1}{2}, \frac{1}{2}$) for F. The antiferromagnetic phase transition in KCoF_3 at $T_N = 115 \text{ K}$ and in RbCoF_3 at $T_N = 101 \text{ K}$ is accompanied by a second-order structural phase transition to the tetragonal phase due to a magnetostrictive distortion as a result of spin-orbit interaction [51,52]. This leads to the 90° antiferromagnetic and structural domains, in which a G -type compensated 3D-Heisenberg antiferromagnetic structure is realized with spins ($S = \frac{3}{2}$) aligned along the tetragonal c axis [52–54]. The irreducible representation analysis using ISODISTORT software [55] gives the tetragonal space group $P4/mmm$ (#123, $Z = 1$), assuming the ferrodistorive phase transition.

Single crystals were grown by the Czochralski method. The x-ray oriented crystals were cut normal to the cubic a axis and therefore three types of structural domains may exist below T_N . Samples for dielectric measurements were prepared in a form of plane-parallel optically polished plates with a thickness about 0.5 mm and area about 10 mm^2 . Measurements of the far-infrared reflectivity spectra were performed on samples with optically polished nonparallel faces with area about 1 cm^2 and thickness about 5 mm . The tetragonal magnetostrictive distortion is very small with $\frac{c-a}{a}$ reaching a value about $-3 \cdot 10^{-3}$ at low temperature [51] and does not

lead to any noticeable splitting or activation of phonons in multidomain crystals [18–20,56]. These observations allow us to consider the anisotropy of the dielectric properties insignificant.

Measurements of the low-frequency dielectric permittivity were done using precision RLC meter AKTAKOM AM-3028 in the frequency range from 20 Hz to 1 MHz. Electric contacts were deposited on the opposite sample faces using silver paint to form a capacitor and annealed at 400 K in vacuum for one hour. Samples were placed in a helium-flow cryostat Cryo CRC-102 and the capacitance measurements were performed at heating with the rate about 1 K/min in the temperature range 5–400 K. Absolute values of the dielectric permittivity were calculated from the capacitance of parallel-plate capacitor. Necessary corrections for the thermal expansion of samples were taken into account for KCoF_3 and RbCoF_3 using the data from Ref. [51]. Experimental data are presented only for the frequency of 100 kHz because no noticeable dispersion was observed in the whole frequency range. The dielectric losses were very small, on the order of 10^{-5} , and no noticeable temperature changes were detected.

The far-infrared reflectivity measurements were carried out with unpolarized incident light at an angle of incidence $\theta \approx 10^\circ$ (i.e., near normal incidence), using a high-resolution Fourier-transform IR spectrometer Bruker IFS 125HR with a liquid-helium-cooled bolometer in the spectral range of 30–700 cm^{-1} . Samples were attached to a cold finger of a closed-cycle helium cryostat Cryomech ST403 and relative reflectivity spectra were measured at continuous cooling from 300 to 5 K with respect to a reference reflectivity of a gold mirror at room temperature. No corrections on the surface quality and shape of the sample, as well as the sample position due to thermal contraction of the cold finger were done. The absolute reflectivity spectra were obtained with a Bruker IFS 66v spectrometer in a spectral range of 50–7500 cm^{-1} at room temperature.

IV. EXPERIMENTAL RESULTS

A. Temperature dependence of the low-frequency dielectric permittivity

Temperature dependence of the low-frequency dielectric permittivity ϵ_0 along the cubic axis is shown by orange line in Figs. 1(a) and 1(b) for KCoF_3 and RbCoF_3 , respectively. Surprisingly, despite the similarities in structural, magnetic, and optical properties of both crystals, these two $\epsilon_0(T)$ dependencies are radically different. The dielectric permittivity in KCoF_3 shows continuous growth with cooling in the whole temperature range with a total relative change of $\Delta\epsilon \approx 3.9\%$. In contrast, $\epsilon_0(T)$ in RbCoF_3 decreases with cooling with $\Delta\epsilon \approx -4.1\%$. Well-defined kinks in the temperature derivatives $d\epsilon/dT$ at T_N obviously related to the antiferromagnetic ordering are observed in both crystals [see Figs. 1(c) and 1(e)]. At room temperature, the absolute value of the low-frequency dielectric permittivity for KCoF_3 is $\epsilon_0 = 7.04$ which is close to that reported in Ref. [18], and for RbCoF_3 $\epsilon_0 = 6.14$.

The temperature dependence of ϵ_0 for KCoF_3 was fitted above T_N by using Eq. (2) with model parameters $\epsilon_B = 6.94$, $C_B = 33.0$, $T_0 = -67.5$ K, and $T_1 = 4$ K. For RbCoF_3 , Eq. (1)

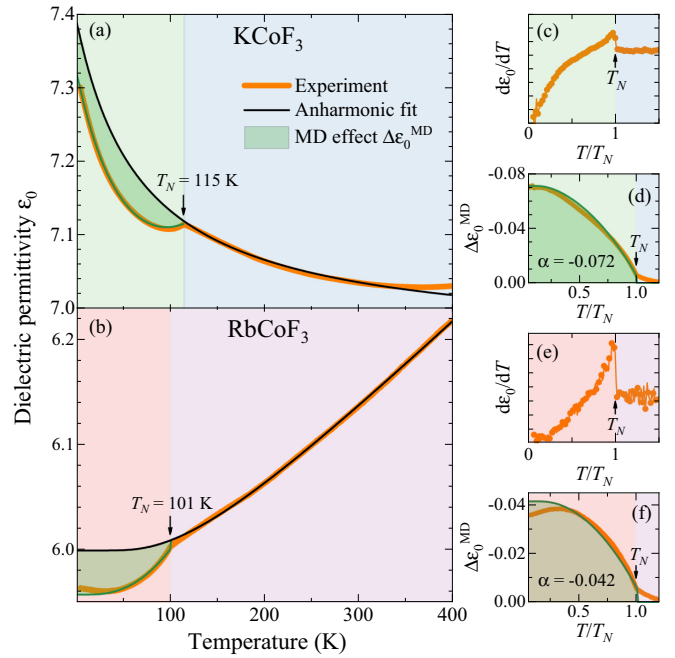


FIG. 1. Temperature dependence of (a), (b) the low-frequency dielectric permittivity ϵ_0 ; (c), (e) the temperature derivative $d\epsilon_0/dT$; and (d), (f) the spontaneous MD effect $\Delta\epsilon_0^{\text{MD}}$ in KCoF_3 and RbCoF_3 , respectively. The black lines are the results of fitting, assuming anharmonic temperature behavior of ϵ_0 in the absence of magnetic ordering. The green lines are fitting results for the dielectric permittivity shift due to the spontaneous MD effect.

was used with parameters $\epsilon_0(0) = 6.00$, $A = 0.31$, and $\omega^* = 246 \text{ cm}^{-1}$. Differences between experimental and fit lines in Figs. 1(a) and 1(b) give the magnetic contribution caused by the spontaneous MD effect $\Delta\epsilon_0^{\text{MD}}$. These differences below T_N were fitted using Eq. (3) as shown by green lines in Figs. 1(d) and 1(f). The value of the spontaneous MD effect accounts to about $\alpha = -0.0718$ (-1.2%) in KCoF_3 and $\alpha = -0.0411$ (-0.6%) in RbCoF_3 . It is interesting to note that regardless of opposite temperature behavior of $\epsilon_0(T)$ in these two crystals, the spontaneous MD effect in both of them is negative.

The radically different temperature behavior of the low-frequency dielectric permittivity ϵ_0 in the two isostructural fluoroperovskites indicates, apparently, the presence of subtle details of their lattice dynamics. To clarify the underlying mechanisms leading to such contrasting behavior of $\epsilon_0(T)$, we undertook the detailed far-infrared spectroscopic study.

B. Temperature dependence of the reflectivity spectra

The group-theoretical analysis of the cubic perovskite structure gives, in total, five triply degenerate modes, $\Gamma_{\text{total}} = 4T_{1u} + T_{2u}$, and after subtracting the acoustic mode T_{1u} and the silent mode T_{2u} , only three IR active modes $\Gamma_{\text{IR}} = 3T_{1u}$ remain [59]. The IR active triply degenerate phonons are split by the Coulomb interaction into nondegenerate LO and doubly degenerate TO phonons.

According to experimental studies [60], lattice dynamical [41,61], and *ab initio* [57] calculations of ionic displacements for cubic fluoroperovskites, the lowest frequency transverse 1TO phonon is assigned to the vibrations of the K or Rb cation

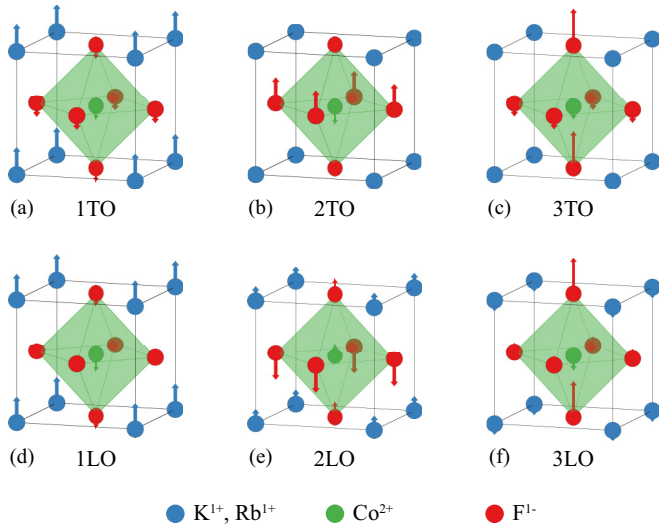


FIG. 2. Schematic diagrams of ionic displacements in the Brillouin zone center for the transverse (a) 1TO, (b) 2TO, (c) 3TO and longitudinal (d) 1LO, (e) 2LO, (f) 3LO phonons in cubic fluoroperovskites according to Ref. [57]. The arrow lengths are normalized in accordance with the corresponding ion displacements. Pictures were prepared using the VESTA software [58].

against the CoF_6 octahedra, as shown in Fig. 2(a). The middle frequency transverse 2TO phonon corresponds to a bending mode with opposite vibrations of the Co^{2+} cation and four planar F^{1-} ions [see Fig. 2(b)]. The highest frequency transverse 3TO phonon is a stretching mode representing predominantly codirectional displacements of two apical fluorides, as shown in Fig. 2(c). We note that there is ambiguity in the literature related to Coulomb interaction regarding bending and stretching modes. Thus, in Refs. [35,62], 2TO is a stretching mode and 3TO is a bending mode whereas in Refs. [41,57,61] the assignment order is reversed. In our paper, we use normal modes in the Brillouin zone center shown in Fig. 2 in accordance with *ab initio* calculations [57]. Since the far-infrared reflectivity spectra contain information not only on transverse but also on longitudinal phonons, Figs. 2(d)–2(f) show displacements of ions for the longitudinal modes 1LO, 2LO, 3LO, respectively. It is worth noting that in cubic oxide perovskites KNbO_3 , BaTiO_3 , and SrTiO_3 , on the contrary, the bending mode has the lowest phonon frequency [60,63].

Figures 3(a) and 3(b) show absolute far-infrared reflectivity spectra at room temperature in KCoF_3 and RbCoF_3 , respectively. The spectra are very similar in their general trends and clearly show the three *reststrahlen* bands in accordance with predictions of the group-theoretical analysis. These bands arise due to the ion displacements and relevant phonons are labeled by the numbers $j = 1-3$ with increasing frequency ω_j as illustrated in Fig. 2. To obtain quantitative information on the lattice dynamics, these spectra were fitted by using Eqs. (4) and (5) with the particle swarm optimization algorithm [64]. Small deviations appear at the highest frequency phonon bands close to 450 cm^{-1} in KCoF_3 and 400 cm^{-1} in RbCoF_3 as seen in Figs. 3(a) and 3(b), respectively. They presumably arise due to multiphonon processes involving zone boundary $\omega_{2\text{TO}}$ and $\omega_{2\text{LO}}$ optical phonons which sum up to a zero-wave vector excitation [20]. The real and imaginary

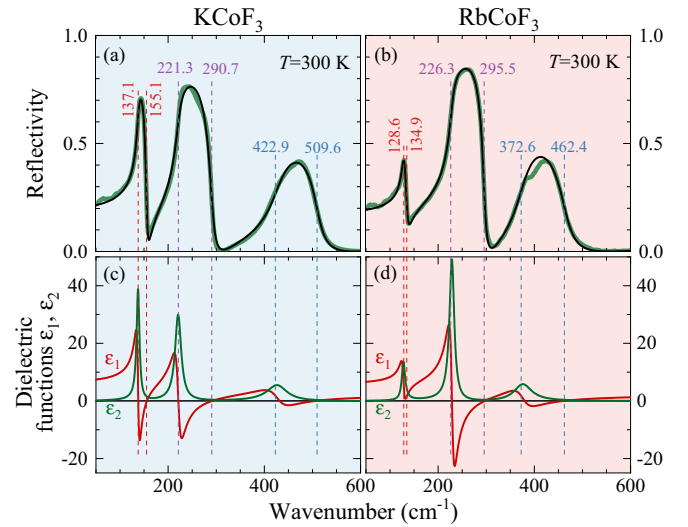


FIG. 3. Absolute far-infrared reflectivity spectra and corresponding real ϵ_1 and imaginary ϵ_2 parts of the dielectric function at room temperature of fluoroperovskites KCoF_3 (a) and (c) and RbCoF_3 (b) and (d), respectively. The black lines are results of fits based on a generalized oscillator model according to Eq. (5). Dashed lines indicate TO and LO phonon frequencies.

parts of the dielectric function $\epsilon(\omega)$ obtained from the fitting analysis are shown in Figs. 3(c) and 3(d) for KCoF_3 and RbCoF_3 , respectively.

Phonon parameters and high-frequency dielectric permittivity ϵ_∞ obtained by fitting the absolute reflectivity spectra at room temperature in the range from 50 to 7500 cm^{-1} are listed in Table I. These parameters are in satisfactory agreement with the literature data for KCoF_3 [18,19] and for RbCoF_3 [65]. The ω_1 phonon frequency for RbCoF_3 is smaller than that for KCoF_3 because in this mode the A ions are displaced against the CoF_6 octahedra as shown in Fig. 2(a) but the Rb^{1+} ion is heavier than the K^{1+} ion. However, the LO-TO splitting of this ω_1 phonon in KCoF_3 is larger than that in RbCoF_3 . The frequency of the ω_2 phonon assigned to the stretching mode F-Co-F [Fig. 2(b)] has approximately the same value in both crystals. The frequency ω_3 of the bending mode $\text{F}_2\text{-Co-F}_2$ [Fig. 2(c)] correlates well with the lattice parameter a similar to other cubic fluoroperovskites [41]. The

TABLE I. Phonon parameters in KCoF_3 and RbCoF_3 at room temperature: frequencies ω_j (cm^{-1}), dampings γ_j (cm^{-1}), dielectric strengths $\Delta\epsilon_j$, and effective plasma frequencies Ω_{jP} (cm^{-1}).

Mode j	$\omega_{j\text{TO}}$	$\gamma_{j\text{TO}}$	$\omega_{j\text{LO}}$	$\gamma_{j\text{LO}}$	$\Delta\epsilon_j$	Ω_{jP}
KCoF_3 ($\epsilon_\infty = 2.18$; $\epsilon_0^{\text{opt}} = 7.01$; $\Omega_{\Sigma P} = 515$)						
1	137.1	7.9	155.1	4.5	2.01	195
2	221.3	16.1	290.7	13.6	2.12	322
3	422.9	60.0	509.6	25.1	0.69	352
RbCoF_3 ($\epsilon_\infty = 2.18$; $\epsilon_0^{\text{opt}} = 6.32$; $\Omega_{\Sigma P} = 497$)						
1	128.6	6.9	134.9	8.0	0.72	109
2	226.3	15.8	295.5	9.2	2.73	374
3	372.6	49.7	462.4	29.0	0.69	309

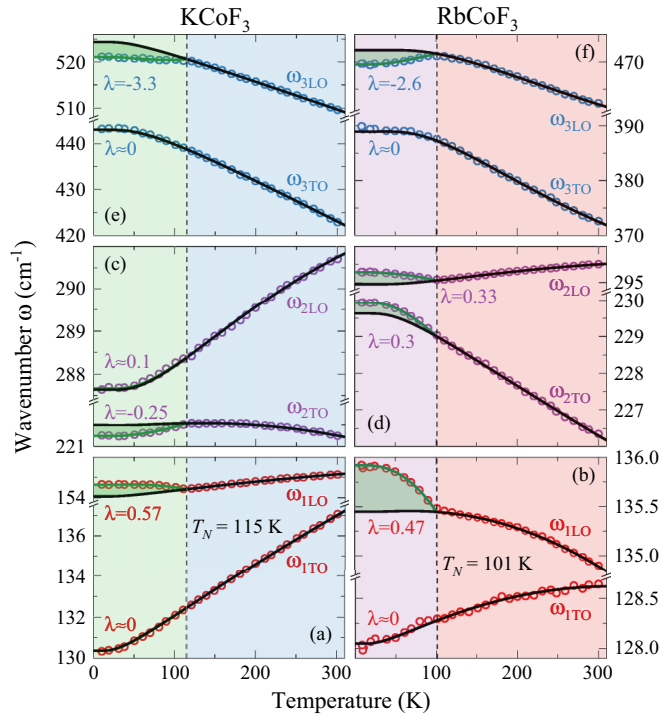


FIG. 4. Temperature dependencies of phonon frequencies for KCoF_3 (left panels) and RbCoF_3 (right panels). The circles correspond to the experimental data. The black lines correspond to the fit of the phonon frequencies under assumption of anharmonic temperature behavior in the absence of magnetic ordering according to Eq. (12). The green lines are fits of the frequency shift due to spin-phonon coupling according to Eq. (14). Values of the spin-phonon coupling constants λ are given for all phonons.

high-frequency dielectric permittivity at room temperature is very close to $\epsilon_\infty = 2.18$ for both crystals.

The relative far-infrared reflectivity spectra at different temperatures were normalized to the absolute spectra at room temperature and the fitting was done as previously described. The fitting of the normalized reflectivity spectra allowed us to obtain absolute values of the TO and LO phonon frequencies $\omega_{j\text{TO}}$ and $\omega_{j\text{LO}}$ only because the high-frequency dielectric permittivity ϵ_∞ and damping γ_j substantially depend on the absolute values of the reflection. Temperature dependencies of phonon frequencies for all IR active modes are shown in Fig. 4 in the range from 5 to 300 K for both crystals. In KCoF_3 , the phonon frequencies span a range from 130 to 522 cm^{-1} and in RbCoF_3 from 128 to 473 cm^{-1} . The changes of the highest frequency ω_3 phonon are more pronounced in comparison to the other phonons as seen in Fig. 4. The TO and LO frequencies of the ω_3 phonon in both crystals have a conventional temperature behavior demonstrating appreciable increase by about 10 cm^{-1} for $\omega_{3\text{LO}}$ and 25 cm^{-1} for $\omega_{3\text{TO}}$ with cooling due to (i) the concomitant phenomena of anharmonic three- and four-phonon processes Eq. (12), which relax the phonon under consideration and renormalize its self-energy, and (ii) lattice thermal expansion which increases the cation-anion bond lengths followed by weakening of the force constants. We note that similar strong hardening of the ω_3 phonon frequency was observed in other nonmagnetic

cubic fluoroperovskites [18,19,35,41,66]. This effect is apparently related to large displacements of the fluorine ions as schematically shown in Figs. 2(c) and 2(f). The longitudinal $\omega_{3\text{LO}}$ phonons reveal distinct negative shifts below T_N due to the antiferromagnetic ordering as shown in Figs. 4(e) and 4(f). Surprisingly, the transversal phonon $\omega_{3\text{TO}}$ does not show any noticeable changes related to the magnetic orderings [see Figs. 4(e) and 4(f)].

The TO phonon frequency $\omega_{2\text{TO}}$ in KCoF_3 slightly hardens with cooling by about 0.5 cm^{-1} with negative shift below T_N while in RbCoF_3 the growth is about 4 cm^{-1} with positive shift due to spin-phonon coupling as shown in Figs. 4(c) and 4(d), respectively. On the other hand, the LO phonon frequency $\omega_{2\text{LO}}$ in KCoF_3 softens by about 4 cm^{-1} , whereas in RbCoF_3 the decrease is about 0.5 cm^{-1} with positive shifts below T_N , as shown in Figs. 4(c) and 4(d).

The largest difference in phonon dynamics between KCoF_3 and RbCoF_3 is observed for the temperature behavior of the lowest frequency ω_1 phonon. In RbCoF_3 , the frequencies show very small changes with temperature and the TO frequency $\omega_{1\text{TO}}$ softens by about 0.6 cm^{-1} whereas LO frequency $\omega_{1\text{LO}}$ hardens about 1 cm^{-1} with positive magnetic shift below T_N as seen in Figs. 4(a) and 4(b), respectively. In contrast, the frequency of the TO mode $\omega_{1\text{TO}}$ in KCoF_3 exhibits a strong downward shift by about 7 cm^{-1} with cooling without any additional shift at magnetic ordering as shown in Fig. 4(a). The LO frequency $\omega_{1\text{LO}}$ in KCoF_3 also slightly softens about 0.6 cm^{-1} with upward shift below T_N [Fig. 4(a)].

The temperature dependencies of phonon frequencies above T_N were fitted according to Eq. (12) to evaluate the influence of the magnetic ordering. There is a good agreement between the fitting results and experimental data except for temperature dependencies of the ω_3 frequencies for which saturation is not observed below 70 K as it follows from Eq. (12) for high frequency phonons, presumably due to their relaxation into two phonons with different frequencies or due to previously described multiphonon processes. These temperature dependencies were fitted using a more simple Eq. (13). The black lines in Fig. 4 correspond to anharmonic contribution to the temperature changes of phonon frequencies. The difference between anharmonic fit lines and experimental data below T_N corresponds to magnetic ordering effects which were fitted using Eq. (14) as shown by the green line in Fig. 4. The values of spin-phonon coupling constant λ which are determined by the second spatial derivatives of the exchange terms [67] are given for all phonons in Fig. 4. We note that in cubic fluoroperovskites the 180° angle of the superexchange pathway dominates over all other exchange interactions [53,68].

It is important to note that frequency shifts due to spin-phonon coupling were observed only for the $\omega_{1\text{LO}}$, $\omega_{2\text{TO}}$, $\omega_{2\text{LO}}$, and $\omega_{3\text{LO}}$ phonons. In all these phonons, the ion displacements change the 180° angle of the superexchange $\text{Co}^{2+} - \text{F}^{1-} - \text{Co}^{2+}$ pathway, thus resulting in modulation of the exchange interaction as shown in Fig. 2 [35,66]. The largest absolute value of $\lambda = -3.3 \text{ cm}^{-1}$ is observed for $\omega_{3\text{TO}}$ frequency for KCoF_3 and $\lambda = -2.6 \text{ cm}^{-1}$ for RbCoF_3 as seen in Figs. 4(e) and 4(f), respectively. For other phonons, the spin-phonon coupling constant is about $\lambda \approx 0.5 \text{ cm}^{-1}$, which is significantly lower than for the IR active phonons

in other magnetic crystals [43,69]. The ω_{1LO} phonon has approximately equal values of the spin-phonon coupling constants in KCoF_3 $\lambda = 0.57 \text{ cm}^{-1}$ and RbCoF_3 $\lambda = 0.67 \text{ cm}^{-1}$. Phonon frequencies ω_{2TO} and ω_{2LO} in RbCoF_3 are about $\lambda \approx 0.3 \text{ cm}^{-1}$ with the same sign while in KCoF_3 the sign of λ for these phonons is opposite. The spin-phonon coupling constant for the ω_{2LO} frequency is small and positive $\lambda \approx 0.1 \text{ cm}^{-1}$, whereas for ω_{2TO} this constant is negative $\lambda = -0.25 \text{ cm}^{-1}$. Temperature dependencies of the ω_{1TO} and ω_{3TO} phonon frequencies with codirectional equal displacements of Co^{2+} ions and planar F^{1-} ions do not show noticeable anomalies below T_N as can be seen in Fig. 4 in both crystals KCoF_3 and RbCoF_3 .

V. ANALYSIS OF RESULTS AND DISCUSSION

The obtained results on phonon frequencies as a function of temperature shown in Fig. 4 open the possibility to reveal the origin of the different temperature behaviors of low-frequency dielectric permittivity in KCoF_3 and RbCoF_3 [see Figs. 1(a) and 1(b)]. The optical static dielectric permittivity in the absence of any microwave excitation should be equal to the low-frequency dielectric permittivity from capacitance measurements. The dielectric strength $\Delta\epsilon$ for all phonons and optical static dielectric permittivity ϵ_0^{opt} were calculated using Eqs. (7) and (8) with the room temperature value of ϵ_∞ and the phonon frequencies at different temperatures. In Ref. [70], it was shown that cubic fluoroperovskites are characterized by very weak temperature changes of ϵ_∞ on the order of $\Delta\epsilon_\infty \approx 5 \cdot 10^{-3}$ in the range of 300 K and in our calculations these changes were neglected.

Determined values of $\Delta\epsilon_j$ and ϵ_∞ for all phonons at room temperature are given in Table I. The first and second phonons in KCoF_3 have approximately equal dielectric strength about $\Delta\epsilon_{1,2} \approx 2.0$ which is higher than the value $\Delta\epsilon_3 \approx 0.7$ for the third phonon. In RbCoF_3 , the second phonon has dielectric strength about $\Delta\epsilon_2 \approx 2.7$, which is larger than those for other phonons with approximately equal values $\Delta\epsilon_{1,3} \approx 0.7$. The value of the optical static dielectric permittivity at room temperature is $\epsilon_0^{\text{opt}} = 7.01$ for KCoF_3 and $\epsilon_0^{\text{opt}} = 6.32$ for RbCoF_3 . These values are close to the room-temperature low-frequency dielectric permittivity ϵ_0 discussed above and the difference in absolute values is apparently related to inaccuracy in determining the area and thickness of samples.

The temperature dependencies of the dielectric strength $\Delta\epsilon$ for all modes and ϵ_0^{opt} in comparison with the low-frequency dielectric permittivity ϵ_0 are shown in Fig. 5. The temperature behavior of $\Delta\epsilon_3$ and $\Delta\epsilon_2$ is very similar in KCoF_3 and RbCoF_3 as can be seen in Figs. 5(a) and 5(b). With cooling, the values of $\Delta\epsilon_3$ slightly decrease with a pronounced negative spontaneous MD effect below T_N . The dielectric strength $\Delta\epsilon_2$ demonstrates the largest room-temperature value and shows a stronger decrease with cooling. A clearly visible negative spontaneous MD effect is seen in Figs. 5(a) and 5(b). Drastically different behavior is observed for $\Delta\epsilon_1$, which grows rapidly with cooling and has a relatively large value in KCoF_3 while in RbCoF_3 $\Delta\epsilon_1$ only slightly increases. The dielectric strength $\Delta\epsilon_1$ has a positive spontaneous MD effect for both crystals. The reason for this difference in the temperature behavior of $\Delta\epsilon_1$ is the presence in KCoF_3 of the

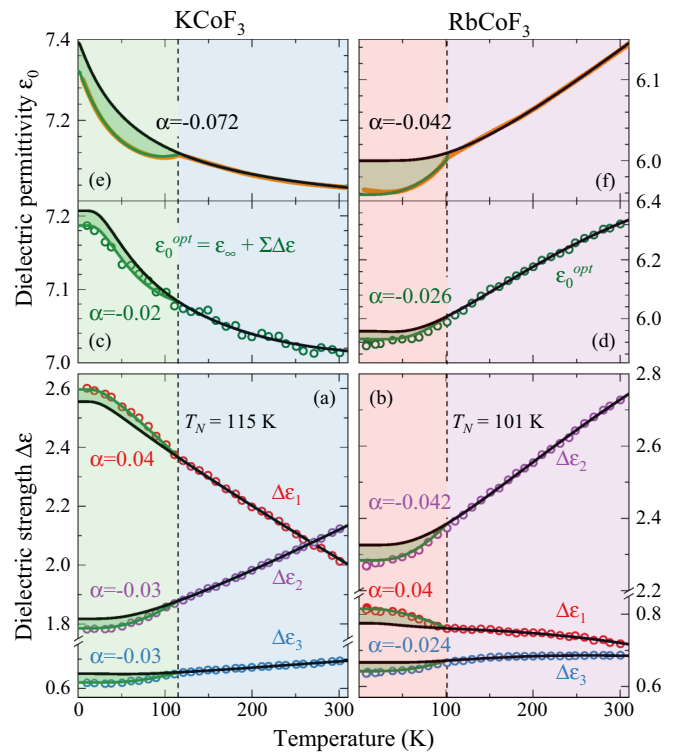


FIG. 5. Temperature dependencies of the dielectric strength $\Delta\epsilon_j$ for all phonons $j = 1-3$ and for the optical static dielectric permittivity ϵ_0^{opt} of KCoF_3 (a), (c) and RbCoF_3 (b), (d). Two upper frames show the temperature dependencies of the low-frequency dielectric permittivity ϵ_0 of KCoF_3 (e) and RbCoF_3 (f). Colored circles correspond to the experimental data. The black and green lines are fits assuming the pure anharmonic effects and the spin-phonon coupling, respectively.

ω_{1TO} phonon, which softens by about 7 cm^{-1} with cooling leading to the increase of LO-TO splitting [see Fig. 4(a)].

Figures 5(c) and 5(d) show the temperature dependence of the optical static dielectric permittivity ϵ_0^{opt} calculated using Eq. (8) for KCoF_3 and RbCoF_3 , respectively. Qualitative agreement is observed between temperature behavior of ϵ_0^{opt} and the low-frequency dielectric permittivity ϵ_0 for both crystals as seen in Figs. 5(c)–5(f). In KCoF_3 , ϵ_0^{opt} increases with cooling over the whole temperature range, whereas in RbCoF_3 , ϵ_0^{opt} continuously decreases. These observations allow us to make an important conclusion, that the anomalous increase of the low-frequency dielectric permittivity ϵ_0 in KCoF_3 with cooling is due to a strong increase of the dielectric strength $\Delta\epsilon_1$. No such effect is present in RbCoF_3 in which the temperature dependence of ϵ_0 is predominantly determined by the changes of $\Delta\epsilon_2$ which are decreased with cooling. It is worth noting that the value of $\omega^* = 246 \text{ cm}^{-1}$ obtained from fitting of $\epsilon_0(T)$ dependence for RbCoF_3 is close to the TO and LO frequencies of the dominant ω_2 phonon. The discrepancies between the temperature dependencies of the optical static and low-frequency dielectric permittivities could apparently arise due to some inaccuracy of phonon frequencies obtained from the fitting of the normalized IR reflectivity spectra.

Dielectric properties of crystals are mainly defined by phonons and therefore it is reasonable to assume that the

drastically opposite temperature changes of the low-frequency dielectric permittivity in isostructural KCoF_3 and RbCoF_3 shown in Figs. 1(a) and 1(b) are related to some fine differences in their lattice dynamics due to different ionic radii of K^{1+} (1.33 Å) and Rb^{1+} (1.47 Å), which results in different values of their tolerance factor t . In fact, the value $t = 0.94$ for KCoF_3 is exactly in the middle of the cubic structure stability range ($0.88 < t < 1.00$) and its crystal structure might supposedly be considered as very stable. Nevertheless, the persistent growth of the low-frequency dielectric permittivity $\epsilon_0(T)$ with cooling is clear evidence of a ferroelectric instability. Replacing K^{1+} (1.33 Å) by Na^{1+} (0.97 Å) leads to the orthorhombic antiferromagnet NaCoF_3 with $t = 0.81$. In contrast, the value $t = 1.00$ for RbCoF_3 falls exactly at the boundary between the cubic and hexagonal crystal structures but, nevertheless, the cubic structure is preserved. The hexagonal crystal structure is observed when Co^{2+} (0.72 Å) is partially substituted by Mg^{2+} (0.66 Å) in $\text{RbCo}_{1-x}\text{Mg}_x\text{F}_3$ ferrimagnet [71].

It deserves mentioning that a similar increase of the optical static or low-frequency dielectric permittivity with cooling is also observed in several nonmagnetic cubic fluoroperovskites RbCaF_3 ($t = 0.88$) [41], CsCaF_3 ($t = 0.94$) [41], KZnF_3 ($t = 0.95$) [41], and in antiferromagnetic RbMnF_3 ($t = 0.96$) [17] with a value of the tolerance factor close or smaller than that in KCoF_3 ($t = 0.94$). Such a trend might be an indication that a similar softening of the lowest frequency TO phonon takes place in cubic fluoroperovskites with $t < 0.97$. It is worth noting that cubic fluoroperovskites have a general tendency toward the lattice instability at the R ($\frac{1}{2}, \frac{1}{2}, \frac{1}{2}$) point of the Brillouin zone, which was experimentally observed in RbCaF_3 , KMnF_3 ($t = 0.91$), CsCaF_3 , and KZnF_3 [72,73]. In fact, we observed a growth of the dielectric permittivity in KZnF_3 ($t = 0.95$) similar to that in KCoF_3 (not shown here). In contrast, a decrease of the low-frequency dielectric permittivity with cooling similar to that in RbCoF_3 is also observed in hexagonal CsMnF_3 ($t = 1.03$) [17]. Apparently, the lattice dynamics is extremely sensitive to the value of the tolerance factor t in fluoroperovskites as predicted in Ref. [14] on the basis of *ab initio* calculations.

For determining the influence of spontaneous MD effect on the dielectric strength and optical dielectric permittivity, we separated pure anharmonic and magnetic contributions using Eqs. (5) and (8) with phonon fit parameters. These contributions are shown by black and green lines in Fig. 5. Spontaneous MD coefficients α have small values about 0.03 for all dielectric strength in both KCoF_3 and RbCoF_3 , as indicated in Fig. 5. The α coefficient of the first dielectric strength $\Delta\epsilon_1$ has a positive sign whereas this coefficient is negative for the second and third phonon, as shown in Figs. 5(a) and 5(b). By summing up the spontaneous MD coefficients of all phonons, we obtain a negative value α of the optical static dielectric permittivity. This result is in agreement with the data for low-frequency dielectric permittivity as can be seen in Figs. 5(e) and 5(f) in both crystals. We note that the agreement between the spontaneous MD effect on the optical static and low-frequency dielectric permittivities is only qualitative because the relevant spontaneous MD coefficients α for each phonon have close absolute values but different signs as shown in Figs. 5(a) and 5(b). It is also worth noting that the

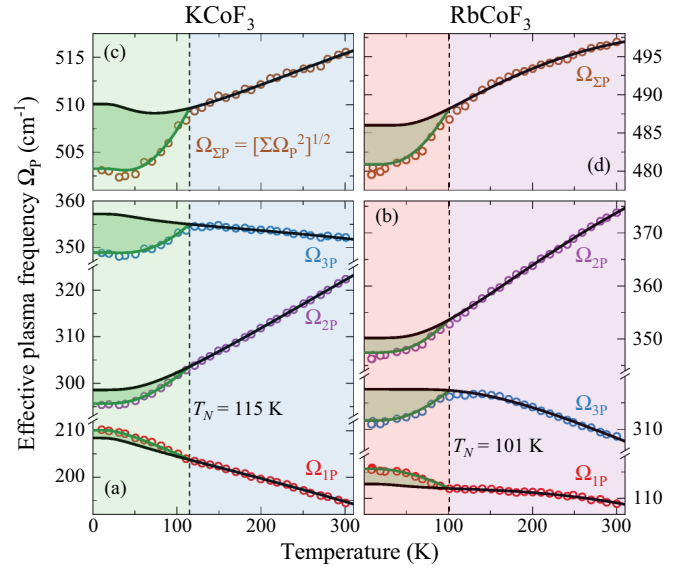


FIG. 6. Temperature dependencies of the effective ionic plasma frequencies Ω_{jP} for all phonons $j = 1-3$ for KCoF_3 (left frames) and RbCoF_3 (right frames). The green and black lines show the fitted temperature dependencies of effective plasma frequencies with and without magnetic ordering, respectively.

temperature dependencies of the spontaneous MD effect for all dielectric strength in both crystals have a M^2 functionality and are well described by using Eq. (3).

We calculated the effective ionic plasma frequencies Ω_P using experimental phonon frequencies and Eqs. (9) and (10) which, ignoring the thermal expansion, depend only on the ion effective charges of KCoF_3 and RbCoF_3 . Figure 6 shows the temperature dependencies of Ω_{jP} for $j = 1-3$ phonons and the sum over all effective plasma frequencies $\Omega_{\Sigma P}$ as colored circles. In KCoF_3 , the room-temperature value of Ω_{jP} increases with increasing phonon frequency, whereas in RbCoF_3 the room-temperature value of Ω_{2P} exceeds Ω_{3P} and Ω_{1P} . Despite the fact that effective ionic plasma frequencies Ω_{jP} are significantly different at room temperature, the total frequency $\Omega_{\Sigma P}$ differs only slightly, as shown in Table I. Temperature dependencies of anharmonic and magnetic contributions to the effective ionic plasma frequencies were calculated using phonon fitting parameters and they are shown in Fig. 6 as black and green lines, respectively. It is seen that the magnetic ordering influences on the effective plasma frequency Ω_{jP} , similar to such effects for the dielectric strength $\Delta\epsilon_j$ of all phonons $j = 1-3$. It is worth noting that the frequency shift $\Omega_{\Sigma P}$ below T_N due to magnetic ordering is not related with a volume change, since the phase transition does not cause a sharp change in the unit cell volume in cobalt fluoroperovskites [51].

We can directly calculate the effective plasma frequencies using Eq. (10) with the assumption of the nominal valencies Z with $\text{K}^{1+}/\text{Rb}^{1+}$, Co^{2+} , and F^{1-} . At room temperature, these frequencies are $\Omega_{\Sigma P} = 632 \text{ cm}^{-1}$ for KCoF_3 and $\Omega_{\Sigma P} = 602 \text{ cm}^{-1}$ for RbCoF_3 . Comparing calculated effective plasma frequency with the experimental $\Omega_{\Sigma P}$ from Table I, we can state that the overall ionicities of both crystals are very close, namely 81.5% for KCoF_3 and 82.6% for RbCoF_3 under the

assumption that the normal valency would produce 100% ionic bond. Equations (10) and (11) have three unknown quantities and therefore do not allow us to uniquely determine the effective ionic charges. But from the overall ionicities, we can conclude that the effective ionic charges in KCoF_3 and RbCoF_3 , in contrast to the oxide perovskites [74], are slightly less than nominal Born effective charges and close to the effective ionic charges in other cubic fluoroperovskites [75].

VI. CONCLUDING REMARKS

In this paper, we presented and analyzed results on detailed experimental studies of the low-frequency dielectric permittivity and far-infrared reflectivity of the model cubic antiferromagnetic fluoroperovskites KCoF_3 and RbCoF_3 . To get better understanding of lattice and magnetic contributions to the phonon dynamics, the measurements were performed in a broad temperature range which includes the antiferromagnetic transition at $T_N = 115$ K and 101 K, respectively. Drastically different temperature behavior of the low-frequency dielectric permittivity ϵ_0 was observed in KCoF_3 and RbCoF_3 , which possess similar structural, magnetic, optical, and other properties. The dielectric permittivity in KCoF_3 shows continuous growth with cooling in the whole temperature range with a total relative change of $\Delta\epsilon_0 \approx 3.9\%$. In contrast, $\epsilon_0(T)$ in RbCoF_3 decreases with $\Delta\epsilon_0 \approx -4.1\%$.

Analysis of the far-infrared reflectivity spectra allowed us to determine the temperature evolution of the all IR active TO and LO phonon frequencies. On the basis of these data, we calculated the dielectric strengths of phonons as a function of temperature. It is demonstrated that in both crystals the temperature behavior of the low-frequency dielectric permittivity is determined by the sum over all phonon dielectric strengths.

We showed that the anomalous growth of the low-frequency dielectric permittivity in KCoF_3 with cooling is explained by the increase of the LO-TO splitting of the lowest frequency $\omega_{\text{LO-TO}}$ phonon caused by its softening of about 7 cm^{-1} . We note that similar anomalous softening of the lowest frequency TO phonon and the increase of the low-

frequency dielectric permittivity were also observed in some other cubic fluoroperovskites which possess values of the tolerance factor t close to that in KCoF_3 . These observations allow us to conclude the existence of the ferroelectric lattice instability in the cubic fluoroperovskites.

The spontaneous MD effect is clearly manifested on the temperature dependence of the low-frequency dielectric permittivity below T_N in both crystals. We attribute this effect to the spin-phonon coupling which leads to frequency shifts of only those IR active TO and LO phonons that change the 180° angle of the superexchange $\text{Co}^{2+} - \text{F}^{1-} - \text{Co}^{2+}$ pathway thus resulting in modulation of the exchange interaction.

We found that the overall ionicity as determined from the summed ionic plasma frequencies $\Omega_{\Sigma\text{P}}$ is 81.5% for KCoF_3 and 82.6% for RbCoF_3 under the assumption that the nominal valency would produce 100% ionic bonds. Thus, we can conclude that the effective ionic charges in KCoF_3 and RbCoF_3 , in contrast to the oxide perovskites [74], are slightly smaller than the nominal Born effective charges and close to the effective ionic charges in other cubic fluoroperovskites [75].

The understanding of the relation between the macroscopic low-frequency dielectric permittivity and phonons, as well as microscopic mechanism of their changes via lattice dynamics induced by magnetic ordering in model cubic antiferromagnets KCoF_3 and RbCoF_3 , provides new insight into the magnetodielectric coupling in magnetic and multiferroic materials. We believe that the suggested approach can be extended to other materials with a more complex crystal structure than that in cubic perovskites.

ACKNOWLEDGMENTS

We are grateful to S. A. Kizhaev, A. K. Tagantsev, and E. A. Vinogradov for useful discussions. We thank O. A. Alekseeva, D. A. Andronikova, and M. P. Scheglov for help in samples preparation. The lattice dynamics study and analysis were funded by Russian Science Foundation according to Project No. 16-12-10456. The dielectric study was funded by Russian Foundation for Basic Research according to Project No. 19-02-00457.

-
- [1] R. J. D. Tilley, *Perovskites: Structure-Property Relationships* (John Wiley & Sons, Chichester, West Sussex, UK, 2016).
 - [2] Y. Moritomo, A. Asamitsu, H. Kuwahara, and Y. Tokura, *Nature* **380**, 141 (1996).
 - [3] D. Cox, B. Noheda, G. Shirane, Y. Uesu, K. Fujishiro, and Y. Yamada, *Appl. Phys. Lett.* **79**, 400 (2001).
 - [4] R. E. Cohen, *Nature* **358**, 136 (1992).
 - [5] Z. B. Guo, Y. W. Du, J. S. Zhu, H. Huang, W. P. Ding, and D. Feng, *Phys. Rev. Lett.* **78**, 1142 (1997).
 - [6] M. Fiebig, T. Lottermoser, D. Meier, and M. Trassin, *Nat. Rev. Mater.* **1**, 16046 (2016).
 - [7] G. Srinivasan, E. T. Rasmussen, B. J. Levin, and R. Hayes, *Phys. Rev. B* **65**, 134402 (2002).
 - [8] Y. Maeno, H. Hashimoto, K. Yoshida, S. Nishizaki, T. Fujita, J. Bednorz, and F. Lichtenberg, *Nature* **372**, 532 (1994).
 - [9] W. S. Yang, J. H. Noh, N. J. Jeon, Y. C. Kim, S. Ryu, J. Seo, and S. I. Seok, *Science* **348**, 1234 (2015).
 - [10] A. Tressaud and K. R. Poeppelmeier, *Photonic and Electronic Properties of Fluoride Materials: Progress in Fluorine Science Series* (Elsevier, Amsterdam, 2016).
 - [11] T.-C. Sum and N. Mathews, *Halide Perovskites: Photovoltaics, Light Emitting Devices, and Beyond* (Wiley-VCH, Weinheim, 2019).
 - [12] The Goldschmidt tolerance factor t is a dimensionless number defined as $t = \frac{r_A + r_F}{\sqrt{2}(r_M + r_F)}$, where r_A , r_M , and r_F are ionic radii and which is used for predicting the stability of the fluoroperovskite structure.
 - [13] D. Babel, in *Structural Chemistry of Octahedral Fluorocomplexes of the Transition Elements*, edited by C. K. Jørgensen, J. B. Neilands, R. S. Nyholm, D. Reinen, R. J. P. Williams, Structure and Bonding, Vol. 3 (Springer, Berlin, Heidelberg, 1967), pp. 1–87.
 - [14] A. C. Garcia-Castro, N. A. Spaldin, A. H. Romero, and E. Bousquet, *Phys. Rev. B* **89**, 104107 (2014).

- [15] A. C. Garcia-Castro, A. H. Romero, and E. Bousquet, *Phys. Rev. Lett.* **116**, 117202 (2016).
- [16] M. Yang, A. KC, A. C. Garcia-Castro, P. Borisov, E. Bousquet, D. Lederman, A. H. Romero, and C. Cen, *Sci. Rep.* **7**, 7182 (2017).
- [17] R. M. Dubrovin, S. A. Kizhaev, P. P. Syrnikov, J.-Y. Gesland, and R. V. Pisarev, *Phys. Rev. B* **98**, 060403(R) (2018).
- [18] J. D. Axe and G. D. Pettit, *Phys. Rev.* **157**, 435 (1967).
- [19] C. H. Perry and E. F. Young, *J. Appl. Phys.* **38**, 4616 (1967).
- [20] K. F. Young and H. P. R. Frederikse, *J. Appl. Phys.* **40**, 3115 (1969).
- [21] D. L. Fox, D. R. Tilley, J. F. Scott, and H. J. Guggenheim, *Phys. Rev. B* **21**, 2926 (1980).
- [22] M. S. Seehra and R. E. Helmick, *Phys. Rev. B* **24**, 5098 (1981).
- [23] M. S. Seehra and R. E. Helmick, *J. Appl. Phys.* **55**, 2330 (1984).
- [24] M. S. Seehra, R. E. Helmick, and G. Srinivasan, *J. Phys. C* **19**, 1627 (1986).
- [25] J. K. Harada, L. Balhorn, J. Hazi, M. C. Kemei, and R. Seshadri, *Phys. Rev. B* **93**, 104404 (2016).
- [26] R. P. Lowndes and D. H. Martin, *Proc. R. Soc. London, Ser. A: Math. Phys. Sci.* **316**, 351 (1970).
- [27] R. A. Bartels and P. A. Smith, *Phys. Rev. B* **7**, 3885 (1973).
- [28] M. Wintersgill, J. Fontanella, C. Andeen, and D. Schuele, *J. Appl. Phys.* **50**, 8259 (1979).
- [29] J. K. Vassiliou, *J. Appl. Phys.* **59**, 1125 (1986).
- [30] K. A. Müller and H. Burkard, *Phys. Rev. B* **19**, 3593 (1979).
- [31] T. Katsufuji and H. Takagi, *Phys. Rev. B* **64**, 054415 (2001).
- [32] J. H. Barrett, *Phys. Rev.* **86**, 118 (1952).
- [33] I. Hatta and N. Sugimoto, *J. Phys. Soc. Jpn.* **49**, 1000 (1980).
- [34] M. I. Darby, *Br. J. Appl. Phys.* **18**, 1415 (1967).
- [35] Y. Tomono, T. Takaoka, M. Yajima, Y. Tanokura, and N. Jinda, *J. Phys. Soc. Jpn.* **59**, 579 (1990).
- [36] G. Lawes, T. Kimura, C. M. Varma, M. A. Subramanian, N. Rogado, R. J. Cava, and A. P. Ramirez, *Prog. Solid State Chem.* **37**, 40 (2009).
- [37] T. Katsufuji, S. Mori, M. Masaki, Y. Moritomo, N. Yamamoto, and H. Takagi, *Phys. Rev. B* **64**, 104419 (2001).
- [38] M. Born and E. Wolf, *Principles of Optics: Electromagnetic Theory of Propagation, Interference and Diffraction of Light*, 7th ed. (Cambridge University Press, Cambridge, 1999).
- [39] F. Gervais and B. Piriou, *J. Phys. C* **7**, 2374 (1974).
- [40] R. H. Lyddane, R. G. Sachs, and E. Teller, *Phys. Rev.* **59**, 673 (1941).
- [41] C. Ridou, M. Rousseau, and F. Gervais, *J. Phys. C* **19**, 5757 (1986).
- [42] S. Kamba, D. Nuzhnyy, P. Vaněk, M. Savinov, K. Knížek, Z. Shen, E. Šantavá, K. Maca, M. Sadowski, and J. Petzelt, *Europhys. Lett.* **80**, 27002 (2007).
- [43] T. Rudolf, C. Kant, F. Mayr, J. Hemberger, V. Tsurkan, and A. Loidl, *Phys. Rev. B* **76**, 174307 (2007).
- [44] F. Gervais and H. Arend, *Z. Phys. B* **50**, 17 (1983).
- [45] J. F. Scott, *Phys. Rev. B* **4**, 1360 (1971).
- [46] M. Balkanski, R. F. Wallis, and E. Haro, *Phys. Rev. B* **28**, 1928 (1983).
- [47] T. Lan, X. Tang, and B. Fultz, *Phys. Rev. B* **85**, 094305 (2012).
- [48] R. A. Cowley, *Adv. Phys.* **12**, 421 (1963).
- [49] M. Cottam and D. Lockwood, *Low Temp. Phys.* **45**, 78 (2019).
- [50] A. Okazaki and Y. Suemune, *J. Phys. Soc. Jpn.* **16**, 671 (1961).
- [51] J. Julliard and J. Nouet, *Rev. Phys. Appl.* **10**, 325 (1975).
- [52] A. Oleaga, A. Salazar, and D. Skrzypczek, *J. Alloys Compd.* **629**, 178 (2015).
- [53] V. Scatturin, L. Corliss, N. Elliott, and J. Hastings, *Acta Crystallogr.* **14**, 19 (1961).
- [54] J. Ferré, B. Briat, R. H. Petit, R. V. Pisarev, and J. Nouet, *J. Phys.* **37**, 503 (1976).
- [55] H. T. Stokes, D. M. Hatch, B. J. Campbell, and D. E. Tanner, *J. Appl. Crystallogr.* **39**, 607 (2006).
- [56] T. M. Holden, W. J. L. Buyers, E. C. Svensson, R. A. Cowley, M. T. Hutchings, D. Hukin, and R. W. H. Stevenson, *J. Phys. C* **4**, 2127 (1971).
- [57] K. Persson, Materials data on KZnF₃ (SG:221) by materials project, an optional note (2014), doi:10.17188/1277157.
- [58] K. Momma and F. Izumi, *J. Appl. Crystallogr.* **44**, 1272 (2011).
- [59] E. Kroumova, M. I. Aroyo, J. M. Perez-Mato, A. Kirov, C. Capillas, S. Ivantchev, and H. Wondratschek, *Phase Transitions* **76**, 155 (2003).
- [60] J. Harada, J. Axe, and G. Shirane, *Acta Crystallograph. Sec. A* **26**, 608 (1970).
- [61] I. Nakagawa, *Spectrochim. Acta, Part A* **29**, 1451 (1973).
- [62] I. Nakagawa, *Appl. Spectrosc. Rev.* **8**, 229 (1974).
- [63] J. Hlinka, J. Petzelt, S. Kamba, D. Noujmi, and T. Ostapchuk, *Phase Transit.* **79**, 41 (2006).
- [64] J. Kennedy and R. Eberhart, *Proceedings of the IEEE International Conference on Neural Networks* (IEEE, Perth, Australia, 1995), Vol. 4, pp. 1942–1948.
- [65] A. P. Lane, D. W. A. Sharp, J. M. Barraclough, D. H. Brown, and D. A. Paterson, *J. Chem. Soc. A* **94** (1971).
- [66] K. Sintani, Y. Tomono, A. Tsuchida, and K. Siratori, *J. Phys. Soc. Jpn.* **25**, 99 (1968).
- [67] E. Granado, A. García, J. A. Sanjurjo, C. Rettori, I. Torriani, F. Prado, R. D. Sánchez, A. Caneiro, and S. B. Oseroff, *Phys. Rev. B* **60**, 11879 (1999).
- [68] L. De Jongh and R. Block, *Physica B + C* **79**, 568 (1975).
- [69] R. Schleck, Y. Nahas, R. P. S. M. Lobo, J. Varignon, M. B. Lepetit, C. S. Nelson, and R. L. Moreira, *Phys. Rev. B* **82**, 054412 (2010).
- [70] P. A. Markov, R. V. Pisarev, G. A. Smolensky, and P. P. Syrnikov, *Solid State Commun.* **19**, 185 (1976).
- [71] M. W. Shafer and T. R. McGuire, *J. Phys. Chem. Solids* **30**, 1989 (1969).
- [72] N. Lehner, H. Rauh, K. Strobel, R. Geick, G. Heger, J. Bouillot, B. Renker, M. Rousseau, and W. Stirling, *J. Phys. C* **15**, 6545 (1982).
- [73] C. Ridou, M. Rousseau, J. Bouillot, and C. Vettier, *J. Phys. C* **17**, 1001 (1984).
- [74] W. Zhong, R. D. King-Smith, and D. Vanderbilt, *Phys. Rev. Lett.* **72**, 3618 (1994).
- [75] K. Wakamura and T. Arai, *Phys. Rev. B* **24**, 7371 (1981).